Nanoscale
Advances

ROYAL SOCIETY
OF CHEMISTRY

PAPER

View Article Online
View Journal | View Issue

Check for updates

Cite this: *Nanoscale Adv.*, 2020, **2**, 5883

Interfacial engineering with carbon–graphite–$Cu_{\delta}Ni_{1-\delta}O$ for ambient-air stable composite-based hole-conductor-free perovskite solar cells†

Yousheng Wang, * Yuzhao Yang, Shaohang Wu, Cuiling Zhang, Zhen Wang, Jinlong Hu, Chong Liu, Fei Guo and Yaohua Mai *

Received 13th October 2020
Accepted 1st November 2020

DOI: 10.1039/d0na00852d

rsc.li/nanoscale-advances

Ambient air atmosphere is inimical to organic–inorganic halide perovskites and organic hole transport materials, and is, thus, necessarily avoided during device fabrication. To solve this issue, it is highly desirable to design stable perovskite-based composites and device configurations. Here, fully ambient-air and antisolvent-free-processed, stable and all-inorganic metal-oxide selective contact hole-conductor-free perovskite solar cells (HCF-PSCs) based on perovskite-based composites with an interfacial engineering strategy are reported. The formation of perovskite-based composites by interfacial engineering with carbon–graphite–$Cu_{\delta}Ni_{1-\delta}O$ not only improved interfacial contacts, charge extraction and transport but also passivated trap states of perovskite thin films and charge recombination at the interfaces. Thus, such perovskite composites with interfacial engineering-based HCF-PSCs without encapsulation showed excellent stability by sustaining 94% of initial PCE over 300 days under ambient conditions.

Introduction

Organic–inorganic halide perovskite (OIHP)-based solar cells have recently achieved an astonishing record-high power conversion efficiency (PCE) up to 25.5% just in a decade, which has endowed them with superb potential for next-generation low-cost, easy-to-fabricate, flexible, wearable and semi-transparent photovoltaics (PVs) in the near future.[1–4] However, the poor stability of OIHPs and organic hole transport materials (OHTMs) owing to long time exposure to harsh environmental conditions (*i.e.*, moisture, air, light and heat stress) has threatened to hinder their widespread applications in opto-electronics and energy harvesting. To get closer to commercialization, the long-term operational stability and ambient-air scalable fabrication of perovskite solar cells (PSCs) are of utmost importance.[5–8] Thus, more stable, printable and highly recyclable carbon-based mesoscopic hole-conductor-free PSCs (HCF-PSCs) may become one of the most promising perovskite-based PVs towards rapid commercialization. However, the efficiency of HCF-PSCs still largely lags behind as compared to that of small-molecule OHTM-based PSCs. The unsatisfactory efficiency of HCF-PSCs is mainly ascribed to low hole transport efficiency, high charge recombination, undesired energy band diagram match and imperfect contacts at the interface of the perovskite/carbon electrode as well as poor carbon adhesion and insufficient incident light by carbon electrodes.[9,10] In order to further improve the efficiency of HCF-PSCs, many efforts have been made for developing advanced and stable perovskite composites with organic or inorganic materials[11–21] and designing novel device configurations with the interfacial engineering strategy.[10,22–26]

The perovskite-based composition engineering with a mixed-cation/halide have significantly enhanced optical and electronic properties, electron–hole extraction and transport as well as intrinsic hybrid-perovskite structure stability.[12–15,27–29] Han *et al.* pioneered HCF-PSCs based on mixed-cation or mixed-halide perovskites ($(5\text{-AVA})_xMA_{1-x}PbI_{3-y}(BF_4)_y$, 5-AVA: 5-aminovaleric acid) by controlling the ratio of two cations or halides, thus endowing the corresponding cells with an improved PCE over 12% and operational stability.[12,13] Interestingly, Grancini *et al.* showed that ultra-stable 2-dimensional/3-dimensional (2D/3D) perovskite-based composites (*i.e.*, $(HOOC(CH_2)_4NH_3)_2PbI_4/MAPbI_3$) could be formed *via* 5-AVAI composition engineering. The 2D/3D perovskite composite-based HCF-PSCs and modules have shown excellent stability over one year.[15] For the development of perovskite composites with organic or inorganic materials, Wang *et al.*[16] reported efficient and stable HCF-PSC-based perovskite-composites with a configuration of FTO/c-TiO_2/mp-TiO_2/$MAPbI_3$–NiO composite/Au. The $MAPbI_3$–NiO composites can effectively facilitate charge carrier generation by

---

Institute of New Energy Technology, College of Information Science and Technology, Jinan University, Guangzhou 510632, China. E-mail: wangys0120@jnu.edu.cn; yaohuamai@jnu.edu.cn

† Electronic supplementary information (ESI) available: FESEM images of Al_2O_3 and $Cu_{\delta}Ni_{1-\delta}O$ NPs, device performance parameters in tables, *J–V* plots, EIS spectra, *J–V* plots of stability test and UV-vis absorption. See DOI: 10.1039/d0na00852d

improving photo-absorption and faster extraction of holes from perovskite to the Au electrode by NiO NPs. Hou *et al.*[18] fabricated perovskite composite-based (*i.e.*, $MAPbI_3$–GuCl and guanidinium chloride) HCF-PSC with a higher open-circuit voltage (V_{oc}) of 1.02 V when compared to pristine $MAPbI_3$-based devices with only 0.88 V. By combining experimental and theoretical studies, the perovskite composites with organic or inorganic materials can significantly enhance the intrinsic stability of perovskite materials *via* strong chemical interactions and bonding or cross-linking as well as using the protective effect of perovskite grains by additive molecules. More importantly, the perovskite composites prepared with cost-effective and environmentally stable inorganic semiconductors, such as NiO nanostructures[16,30–34] and carbon-based nanomaterials,[35–39] have the potential for future commercialization.

The interfacial contacts and properties at the interfaces of the perovskite/electron-transport-layer (perovskite/ETL) and perovskite/electrode are critical for the photovoltaic performance and stability in HCF-PSCs. In particular, except for the degradation of OIHPs themselves, poor stability of the state-of-the-art PSCs can be attributed to interfacial collapse induced by the TiO_2 photocatalysis effect and charge accumulation at the TiO_2/perovskite interface,[40,41] light-induced ion migration and segregation behavior,[42–44] and formation of AuI_2^- or AgI_2^- because of the diffusion of Au or Ag into the perovskite.[45,46] For improving the interface contact between the perovskite layer and top electrode, interfacial engineering has been proposed.[22–26,47–49] Overall, the development of stable perovskite-based composites combined with proper materials and designing novel configuration with interfacial engineering are efficient strategies to achieve highly efficient and stable HCF-PSCs under ambient conditions.

In this study, we report fully-ambient-air and antisolvent-free-processed, highly efficient and stable HCF-PSCs with interfacial engineering-based perovskite composites. The perovskite composites (*i.e.*, $Cu_\delta Ni_{1-\delta}O$–$MAPbI_{3-x}Cl_x$, carbon–graphite (C–G)–$Cu_\delta Ni_{1-\delta}O$–$MAPbI_{3-x}Cl_x$ and Al_2O_3–$MAPbI_{3-x}Cl_x$) were self-formed *via* a one-step deposition of the as-prepared $MAPbI_{3-x}Cl_x$–$Cu_\delta Ni_{1-\delta}O$ mixed-solution on the stacked configuration of FTO/SnO_2/Al_2O_3/$Cu_\delta Ni_{1-\delta}O$/C–G–$Cu_\delta Ni_{1-\delta}O$, where SnO_2 is the ETL and Al_2O_3/$Cu_\delta Ni_{1-\delta}O$/C–G–$Cu_\delta Ni_{1-\delta}O$ is used for interfacial engineering between ETL and the active layer (AL). It was found that $Cu_\delta Ni_{1-\delta}O$ and C–G in the perovskite composites effectively facilitated charge extraction and transport as well as passivated the trap states of perovskite thin films, recombination and ion migration at the interfaces. Furthermore, the multi-stacked SnO_2/Al_2O_3–$MAPbI_{3-x}Cl_x$/$Cu_\delta Ni_{1-\delta}O$–$MAPbI_{3-x}Cl_x$/C–G–$Cu_\delta Ni_{1-\delta}O$–$MAPbI_{3-x}Cl_x$ composite layer effectively reduced the photocurrent density loss and improved interfacial contacts. Finally, the HCF-PSCs based on perovskite composites with interfacial engineering yielded the best PCE of 14.78% with a V_{oc} of 0.95 V, J_{sc} of 23.85 mA cm^{-2} and an FF of 65.23%. More importantly, such perovskite composites with interfacial engineering-based devices showed excellent air, photo- and thermal stability, which are attributed to moisture- and ion migration-sequestration by C–G and strong chemical interactions between $Cu_\delta Ni_{1-\delta}O$ and perovskite molecules.

Results and discussion

The surface morphologies of mesoporous Cu-doped NiO ($Cu_\delta Ni_{1-\delta}O$) and Al_2O_3, and the cross-sectional structure of FTO/SnO_2/Al_2O_3/$Cu_\delta Ni_{1-\delta}O$ were examined *via* field emission scanning electron microscopy (FESEM), clearly showing uniform and mesoporous structures (Fig. S1†). Such thin-film morphologies of metal oxide nanoparticles (MONs) effectively facilitate the perovskite $MAPbI_{3-x}Cl_x$ solution infiltration and increase the contact areas between perovskite molecules and mesoporous MONs (*i.e.*, $Cu_\delta Ni_{1-\delta}O$ and Al_2O_3), leading to the formation of perovskite–MONs composites (*i.e.*, $Cu_\delta Ni_{1-\delta}O$–$MAPbI_{3-x}Cl_x$ and Al_2O_3–$MAPbI_{3-x}Cl_x$). Besides, the surface morphologies of the as-formed C–G–$Cu_\delta Ni_{1-\delta}O$–$MAPbI_{3-x}Cl_x$ composite film are also clearly observed in the FESEM image, as shown in Fig. 1a. Fig. 1d further verifies that the perovskite ($MAPbI_{3-x}Cl_x$) solution readily infiltrated into all the mesoporous layers of C–G–$Cu_\delta Ni_{1-\delta}O$, $Cu_\delta Ni_{1-\delta}O$, and Al_2O_3. It can be seen that all the layers are well-defined with good adhesion to one another, exhibiting the top electrode of Au, the AL of C–G–$Cu_\delta Ni_{1-\delta}O$–$MAPbI_{3-x}Cl_x$, the interfacial layer of Al_2O_3/$Cu_\delta Ni_{1-\delta}O$/C–G–$Cu_\delta Ni_{1-\delta}O$ infiltrated with perovskite molecules and the ETL layer of SnO_2. Fig. 1b shows the device configuration of FTO/SnO_2/Al_2O_3–$MAPbI_{3-x}Cl_x$/$Cu_\delta Ni_{1-\delta}O$–$MAPbI_{3-x}Cl_x$/C–G–$Cu_\delta Ni_{1-\delta}O$–$MAPbI_{3-x}Cl_x$/Au, where the SnO_2 is the ETL and Al_2O_3/$Cu_\delta Ni_{1-\delta}O$/C–G–$Cu_\delta Ni_{1-\delta}O$ is for interfacial engineering between ETL and AL. Such multi-layers of mesoporous configuration remarkably enhance the visible light-harvesting as well as improve J_{sc} (see Table 1 and Fig. 3a). Fig. 1c shows the energy band diagram and blocking properties in HCF-PSCs: (1) $Cu_\delta Ni_{1-\delta}O$ and C–G in the AL have a suitable band energy alignment of the valence band (VB) (−5.3 eV) and (−5.0 eV),

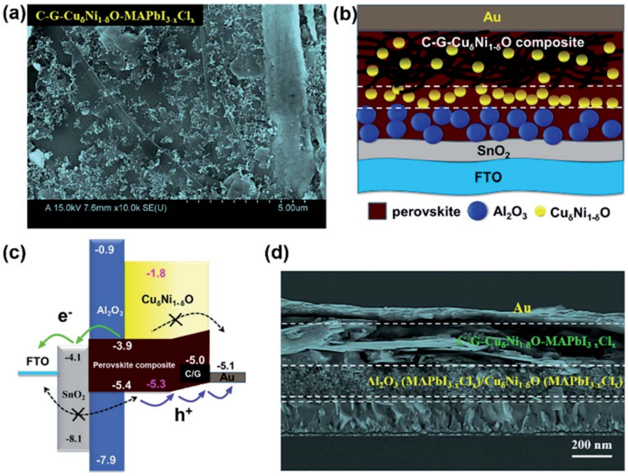

Fig. 1 (a) The surface morphology of the C–G–$Cu_\delta Ni_{1-\delta}O$–$MAPbI_{3-x}Cl_x$ composite film, (b) device configuration, (c) schematic of the energy band diagram and blocking properties and (d) a cross-sectional SEM image for HCF-PSCs of FTO/SnO_2/Al_2O_3/$Cu_\delta Ni_{1-\delta}O$/C–G–$Cu_\delta Ni_{1-\delta}O$–$MAPbI_{3-x}Cl_x$/Au.

Table 1 Photovoltaic parameters of three types of HCF-PSCs: FTO/c-TiO_2/mp-TiO_2/Al_2O_3/$Cu_\delta Ni_{1-\delta}O$/C–G–$MAPbI_{3-x}Cl_x$/Au, FTO/SnO_2/Al_2O_3/$Cu_\delta Ni_{1-\delta}O$/C–G–$MAPbI_{3-x}Cl_x$/Au and FTO/SnO_2/Al_2O_3/$Cu_\delta Ni_{1-\delta}O$/C–G–$Cu_\delta Ni_{1-\delta}O$–$MAPbI_{3-x}Cl_x$/Au. R_s, R_1 and R_2 were measured at 250 mV-applied bias under one sunlight intensity in the range from 1 Hz to 300 kHz by electronic impedance spectroscopy (EIS) measurement

Device configuration	V_{oc} (V)	J_{sc} (mA cm^{-2})	FF (%)	PCE (%)	R_s (Ω)	R_1 (Ω)	R_2 (Ω)
FTO/c-TiO_2/mp-TiO_2/Al_2O_3/$Cu_\delta Ni_{1-\delta}O$/C–G–$MAPbI_{3-x}Cl_x$/Au	0.88	20.97	55.30	10.21	14.5	346	748
FTO/SnO_2/Al_2O_3/$Cu_\delta Ni_{1-\delta}O$/C–G–$MAPbI_{3-x}Cl_x$/Au	0.90	23.01	57.12	11.83	12.2	338	956
FTO/SnO_2/Al_2O_3/$Cu_\delta Ni_{1-\delta}O$/C–G–$Cu_\delta Ni_{1-\delta}O$–$MAPbI_{3-x}Cl_x$/Au	0.95	23.85	65.23	14.78	10.8	245	1078

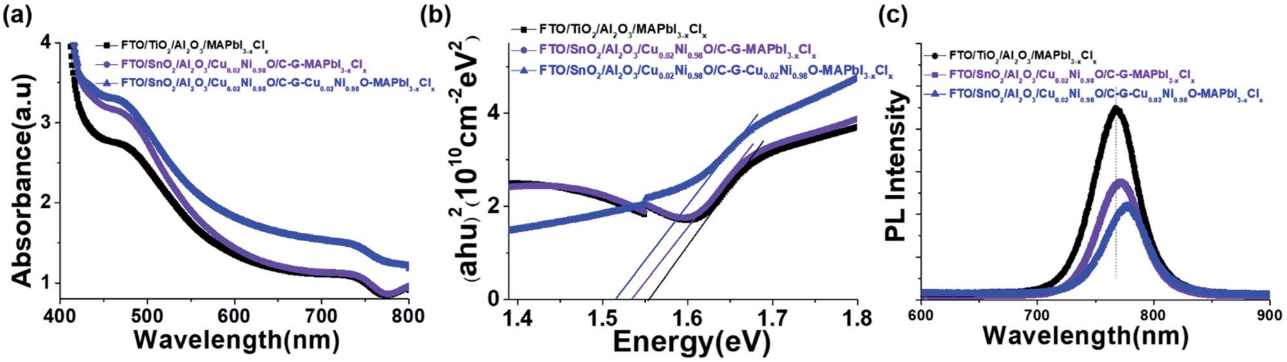

Fig. 2 (a) UV-vis spectra, (b) corresponding Tauc plots and (c) PL spectra for three films: FTO/TiO_2/Al_2O_3/$MAPbI_{3-x}Cl_x$ (dark), FTO/SnO_2/Al_2O_3/$Cu_\delta Ni_{1-\delta}O$/C–G–$MAPbI_{3-x}Cl_x$ (purple) and FTO/SnO_2/Al_2O_3/$Cu_\delta Ni_{1-\delta}O$/C–G–$Cu_\delta Ni_{1-\delta}O$–$MAPbI_{3-x}Cl_x$ (blue).

which is quite close to that of perovskite $MAPbI_{3-x}Cl_x$ (−5.4 eV), leading to fast hole transport; (2) the formation of the C–G–$Cu_\delta Ni_{1-\delta}O$–$MAPbI_{3-x}Cl_x$-graded heterojunction also enhances hole transport but efficiently blocks the electron going to the Au electrode due to electron blocking property of $Cu_\delta Ni_{1-\delta}O$ with a high conduction band (CB) (−1.8 eV); (3) the wide-bandgap Al_2O_3 (~7 eV) plays an important role in hole–electron extraction and recombination suppression by avoiding direct contact between n-type SnO_2 and p-type $Cu_\delta Ni_{1-\delta}O$; (4) highly conductive C–G effectively improves the conductivity and work function of C–G–$Cu_\delta Ni_{1-\delta}O$ composites; (5) defect density of perovskite films are suppressed by the C–G–$Cu_\delta Ni_{1-\delta}O$ interface modification and strong chemical interactions or crosslinking between $Cu_\delta Ni_{1-\delta}O$ and perovskite molecules.[16,30–33,50,51] Upon illumination, the HCF device configuration probably four conduction paths are available for holes: direct transport to the Au electrode, transport to $Cu_\delta Ni_{1-\delta}O$ to the Au electrode, transport to C–G to the Au electrode and transport to $Cu_\delta Ni_{1-\delta}O$ to C–G and finally to the Au electrode. It is believed that SnO_2, Al_2O_3, $Cu_\delta Ni_{1-\delta}O$, and C–G can play individual roles in the effective electron and hole transport. Therefore, such a device configuration with perovskite composites and multi-layer interface engineering not only eliminates undesired interface energy disorder but also results in efficient charge separation and conduction in the AL and at the interfaces, leading to a remarkable improvement of device performance and stability.

To compare the optical and electronic properties of C–G–$Cu_\delta Ni_{1-\delta}O$–$MAPbI_{3-x}Cl_x$ composites, C–G–$MAPbI_{3-x}Cl_x$ composites and pristine perovskite $MAPbI_{3-x}Cl_x$ films, we recorded ultraviolet-visible (UV-vis) spectra and photoluminescence (PL) spectra, as shown in Fig. 2. All films exhibit remarkable light-harvesting absorption from 400 to 800 nm (Fig. 2a). Compared to the absorption of pristine perovskite $MAPbI_{3-x}Cl_x$ and C–G–$MAPbI_{3-x}Cl_x$ films, the C–G–$Cu_\delta Ni_{1-\delta}O$–$MAPbI_{3-x}Cl_x$ composite film shows enhanced light absorption over the entire visible spectrum, resulting in the highest light-harvesting ability. More importantly, such a composite-based film shows an efficient PL quenching and red-shift toward longer wavelengths (Fig. 2c), which is attributed to a reduced band gap from 1.561 to 1.533 eV (Fig. 2b). The fast PL quenching, red-shift and reduced band gap indicate efficient carrier extraction and transport, and suppression of interfacial recombination and trap density, which can remarkably improve solar cell PV parameters (see Table 1 and Fig. 3a).

To evaluate the device performance of C–G-based HCF-PSCs based on perovskite composites with interfacial engineering, we fabricated three C–G-based devices: FTO/c-TiO_2/mp-TiO_2/Al_2O_3/$Cu_\delta Ni_{1-\delta}O$/C–G–$MAPbI_{3-x}Cl_x$/Au (device A, Fig. S2†), FTO/SnO_2/Al_2O_3/$Cu_\delta Ni_{1-\delta}O$/C–G–$MAPbI_{3-x}Cl_x$/Au (device B, Fig. S3†), and FTO/SnO_2/Al_2O_3/$Cu_\delta Ni_{1-\delta}O$/C–G–$Cu_\delta Ni_{1-\delta}O$–$MAPbI_{3-x}Cl_x$/Au (device C, Fig. 1d). Devices B and C incorporated SnO_2 to replace TiO_2 ETL and device C used the C–G–$Cu_\delta Ni_{1-\delta}O$–$MAPbI_{3-x}Cl_x$ composite in AL. It was confirmed that the $Cu_\delta Ni_{1-\delta}O$ optoelectronic properties greatly depend on Cu doping concentrations.[17] Herein, we scrutinized the PV performance of the device A for different concentrations of Cu doping and obtained the best PCE with an optimal content of $\delta = 0.02$ (Fig. S2c and Table S1†). Besides, the thickness of SnO_2 and the concentration of C–G–$Cu_\delta Ni_{1-\delta}O$ composites in HCF-PSCs were also optimized, as shown in Fig. S3c and Table S3.† In conclusion, the incorporation of the C–G–$Cu_\delta Ni_{1-\delta}O$–$MAPbI_{3-x}Cl_x$ composite in AL together with SnO_2, ETL and Al_2O_3/$Cu_\delta Ni_{1-\delta}O$/C–G–$Cu_\delta Ni_{1-\delta}O$

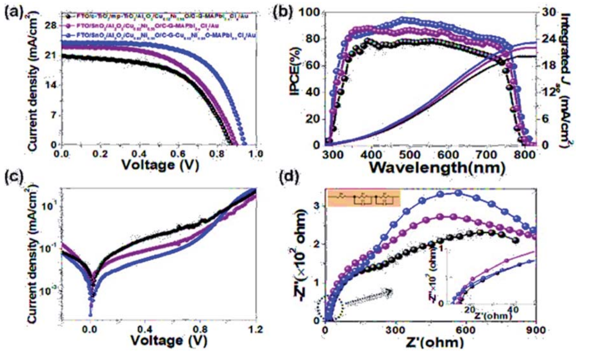

Fig. 3 (a) J–V curves, (b) IPCE spectra with integrated J_{sc}, (c) dark-current, (d) EIS spectra (inset is the enlarged area for dash circle) for HCF-PSCs: FTO/c-TiO_2/mp-TiO_2/Al_2O_3/$Cu_\delta Ni_{1-\delta}O$/C–G–$MAPbI_{3-x}Cl_x$/Au (black), FTO/SnO_2/Al_2O_3/$Cu_\delta Ni_{1-\delta}O$/C–G–$MAPbI_{3-x}Cl_x$/Au (purple) and FTO/SnO_2/Al_2O_3/$Cu_\delta Ni_{1-\delta}O$/C–G–$Cu_\delta Ni_{1-\delta}O$–$MAPbI_{3-x}Cl_x$/Au (blue).

interfacial engineering layers showed the overall best performance for the HCF devices (*i.e.*, a PCE of 14.78% with a V_{oc} of 0.95 V, J_{sc} of 23.85 mA cm^{-2}, and FF of 65%, Table 1). Such enhancement of V_{oc} and J_{sc} is ascribed to the reduced defect-related losses and trap density in materials, desirable energy-level alignment with almost no electron-transport-barrier SnO_2 as ETL, efficient blocking properties of Al_2O_3 and $Cu_\delta Ni_{1-\delta}O$, and formation of a graded heterojunction by perovskite composites. It can be noted that the incident-photon-to-current-efficiency (IPCE) spectrum of the HCF-champion cell (device C) shows the strongest light absorption over a broad wavelength from 350 to 780 nm than that of device A and device B (Fig. 3b). Moreover, the integrated J_{sc} of the HCF-champion cell calculated from the IPCE spectrum was 23.21 mA cm^{-2}, which is in good agreement with the measured J–V curve (23.85 mA cm^{-2}). Fig. 3c clearly shows that the dark current density of the C–G–$Cu_\delta Ni_{1-\delta}O$–$MAPbI_{3-x}Cl_x$ composite-based device is almost one order of magnitude lower than that of the pristine $MAPbI_{3-x}Cl_x$ perovskite-based device. Note that device C shows the lowest series-resistant R_s and charge transfer resistance R_1 of 10.8 and 245 Ω, and highest recombination resistance R_2 of 1078 Ω, which were obtained *via* electronic impedance spectroscopy (EIS) measurements (Fig. 3d and Table 1). Such results indicate that the C–G–$Cu_\delta Ni_{1-\delta}O$–$MAPbI_{3-x}Cl_x$ composite films can not only improve interfacial contacts, charge extraction and transport but also lower the current leakage and charge recombination as well as increase the shunt resistance and longer carrier lifetime.

It was found that compared to TiO_2 ETL devices (device A, black curve), the SnO_2 ETL devices (devices B (red) and C (blue) in Fig. 3a) showed the remarkable enhancement of PCE and photo-stability (Fig. S3d and S5†). Furthermore, we examined how light soaking time affects the PV performance of HCF devices and found that the TiO_2-based device A increased its PV parameters for 90 s and then were gradually decreasing (Fig. S2d and Table S2†). However, the SnO_2-based devices B and C resulted in the substantial improvement of photovoltaic parameters as a function of light soaking time and was stabilized after 200 s (Fig. S3d, S4b, S5, Tables S4 and S6†). Thermal stability is another challenge towards the rapid commercialization of PSCs. Compared to the pristine $MAPbI_{3-x}Cl_x$ with spiro-OMeTAD device (control device), C–G–$Cu_\delta Ni_{1-\delta}O$–$MAPbI_{3-x}Cl_x$ with interfacial engineering-based HCF-PSCs shows excellent thermal-stability at 85 °C under ambient conditions (45–50% humidity) (Fig. S6†). In particular, all PV parameters of the pristine $MAPbI_{3-x}Cl_x$ with HTM spiro-OMeTAD-based cell showed severely deteriorated thermal stability after 120 h, *i.e.*, original PCEs decreased from 18.02% to 7.71% (only retaining 42.8%, Table S7 and Fig. S7a†). However, C–G–$Cu_\delta Ni_{1-\delta}O$–$MAPbI_{3-x}Cl_x$ based on interfacial engineering HCF-PSCs sustained its stability over 120 h by retaining ∼97.8% of its original V_{oc}, ∼92.6% of J_{sc}, ∼99.1% of FF and ∼89.8% of PCE at 85 °C in an ambient environment (45–50% humidity) (Fig. S7b and Table S8†). Furthermore, we examined UV-vis spectrum performance as a function of time for FTO/SnO_2/$MAPbI_{3-x}Cl_x$/spiro-OMeTAD and FTO/SnO_2/Al_2O_3/$Cu_\delta Ni_{1-\delta}O$/C–G–$Cu_\delta Ni_{1-\delta}O$–$MAPbI_{3-x}Cl_x$ films at 85 °C heating in ambient air (humidity 45–50%). The UV-vis spectrum performance clearly shows that the pristine $MAPbI_{3-x}Cl_x$ with the spiro-OMeTAD film totally changed to PbI_2 after 20 days. Adversely, the C–G–$Cu_\delta Ni_{1-\delta}O$–$MAPbI_{3-x}Cl_x$-based film had almost no change (Fig. S8†). To examine the long-term stability of the HCF devices based on C–G–$Cu_\delta Ni_{1-\delta}O$–$MAPbI_{3-x}Cl_x$ with Al_2O_3/$Cu_\delta Ni_{1-\delta}O$/C–G–$Cu_\delta Ni_{1-\delta}O$ interfacial engineering, the target device fabricated by the antisolvent-free strategy was stored under ambient conditions without any encapsulation. Fig. 4 shows the control (pristine $MAPbI_{3-x}Cl_x$ with spiro-OMeTAD-based cell) and the target device (C–G–$Cu_\delta Ni_{1-\delta}O$–$MAPbI_{3-x}Cl_x$-based HCF-cell) of long-term stability as a function of storage days in terms of the normalized performance parameters, *i.e.* V_{oc} (a), J_{sc} (b), FF (c) and PCE (d). Compared to the control device, it can be clearly seen that the normalized performance parameters in the target device are almost not changed in 300 d. More importantly, the target device sustained its stability over 300 days by retaining ∼94% of PCE in an

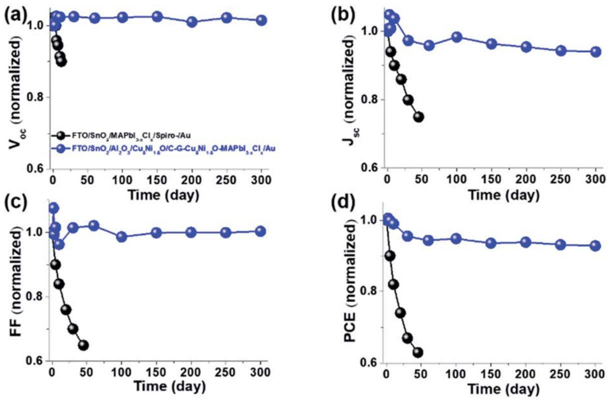

Fig. 4 Long-term stability of FTO/SnO_2/$MAPbI_{3-x}Cl_x$/spiro-OMeTAD/Au (black) and FTO/SnO_2/Al_2O_3/$Cu_\delta Ni_{1-\delta}O$/C–G–$Cu_\delta Ni_{1-\delta}O$–$MAPbI_{3-x}Cl_x$/Au under ambient conditions (45–50% humidity and 25–30 °C).

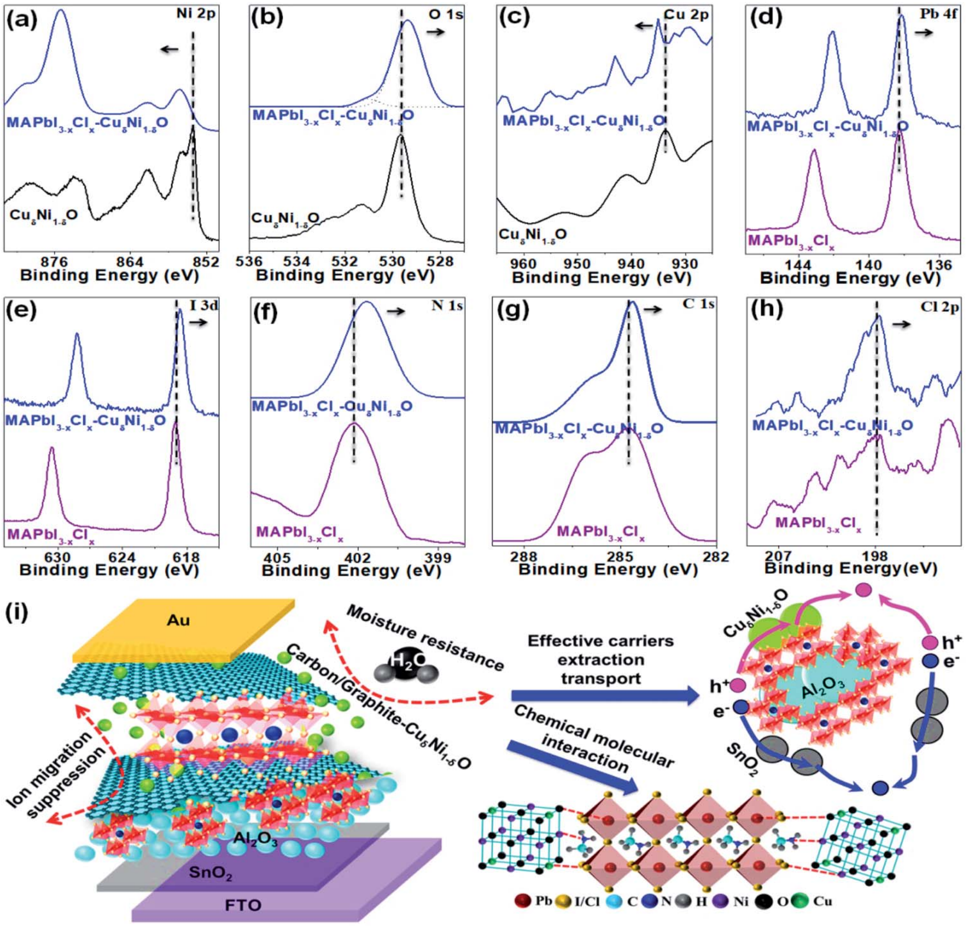

Fig. 5 X-ray photoelectron spectroscopy (XPS) spectra of MAPbI$_{3-x}$Cl$_x$ and MAPbI$_{3-x}$Cl$_x$–Cu$_\delta$Ni$_{1-\delta}$O films: (a) Ni 2p, (b) O 1s, (c) Cu 2p, (d) Pb 4f, (e) I 3d, (f) N 1s, (g) C 1s and (h) Cl 2p. (i) Stability, carrier working mechanisms, and possibility of chemical bonding Ni–I, Ni–Pb, Pb–O–Pb and N–Ni between Cu$_\delta$Ni$_{1-\delta}$O and perovskite material.

ambient environment (45–50% humidity) (Fig. S9 and Table S9†).

By examining XPS data (Fig. 5) on both pristine MAPbI$_{3-x}$Cl$_x$ and composite-based Cu$_\delta$Ni$_{1-\delta}$O–MAPbI$_{3-x}$Cl$_x$ films, the core levels of all components in the Cu$_\delta$Ni$_{1-\delta}$O–MAPbI$_{3-x}$Cl$_x$ film (*i.e.*, O 1s, Pb 4f, I 3d, N 1s, C 1s and Cl 2p) showed a substantial shift towards a lower binding energy compared to the pristine MAPbI$_{3-x}$Cl$_x$ film. Interestingly, the core level of Ni 2p and Cu 2p showed a slight shift towards a higher binding energy, where the nitrogen and iodide or chloride ligands from the MA cation might serve as a ligand bridge to form Ni/Cu–N and Ni/Cu–I or Ni/Cu–Cl bonds, respectively. From the XPS data, it can be concluded that there is a presence of strong chemical interaction and chemical bonding between Cu$_\delta$Ni$_{1-\delta}$O and perovskite, as shown in Fig. 5. In conclusion, such improvement is mainly attributed to the effect of Cu$_\delta$Ni$_{1-\delta}$O and C–G in the perovskite-based composites, which can effectively facilitate charge extraction and transport and interfacial contacts as well as passivation of trap states and recombination in perovskite thin films and at interfaces (also see Fig. 5). The strong chemical interactions and bonding between perovskite and Cu$_\delta$Ni$_{1-\delta}$O elements as well as the presence of C–G in composites also enhance the intrinsic stability of the perovskite materials and interfacial degradation.[16,30–32,52] Moreover, the lattice constant of graphite ($\alpha = 2.46$ Å) is less than the ionic diameter of I/Cl ($d = 4.28$ Å/3.62 Å), which significantly suppresses the halide migration towards the top electrode. In addition, the multi-stacked configuration of SnO$_2$/Al$_2$O$_3$/Cu$_\delta$Ni$_{1-\delta}$O/C–G–Cu$_\delta$Ni$_{1-\delta}$O–MAPbI$_{3-x}$Cl$_x$ can effectively reduce the photocurrent density loss and improve interfacial contacts between perovskite and other layers. Such multi-layer configuration can also effectively improve device air-stability by protecting perovskite molecules from moisture resistance by C–G, and deprotonation and decomposition due to reduction with superoxide (O^{2-}) (Fig. 5). In all, the combined perovskite-based composites and interfacial engineering can lead to substantial performance improvements and operational stability in HCF-PSCs.

Conclusions

In summary, we have achieved fully-ambient-air and antisolvent-free-processed stable hole-conductor-free perovskite solar cells (HCF-PSCs) based on perovskite composites with carbon–graphite (C–G)–Cu$_\delta$Ni$_{1-\delta}$O interfacial engineering.

With the substantial improvement in the perovskite properties, energy-level alignment at the p-type interface between perovskite and C–G–$Cu_{\delta}Ni_{1-\delta}O$ and their interfacial contacts, the perovskite composites with interfacial engineering-based HCF-PSCs yielded a PCE of 14.78% and excellent operational stability. We believe that metal oxides and carbon-based perovskite composites and interfacial engineering can pave the way for designing efficient, large-scale and stable PSCs.

Experimental section

Material preparation

The synthesis of CH_3NH_3I (methylammonium iodide, MAI) was described in our previous works.[16] The preparation of the SnO_2 precursor, Al_2O_3 and $Cu_{\delta}Ni_{1-\delta}O$ NP solutions can be found in our previous works.[30–33] To prepare a solution of $MAPbI_{3-x}Cl_x$–$Cu_{\delta}Ni_{1-\delta}O$ composite, 100 μL 1.5 wt% $Cu_{\delta}Ni_{1-\delta}O$ (2 at% Cu doping) dispersion was added to the perovskite $MAPbI_{3-x}Cl_x$ solution contained by mixing 475 mg MAI and 222 mg lead(II) chloride ($PbCl_2$, 99.999%, Sigma-Aldrich) and 76 mg lead(II) acetate trihydrate ($Pb(CH_3CO_2)_2\cdot 3H_2O$, 99.999%, Sigma-Aldrich) in 1 mL dimethylformamide, followed by ultrasonication for 30 min and continuously stirring for 24 h under ambient conditions (45–50% humidity and 25–30 °C).

Device fabrication

All the fabrication processes of PSCs were carried out *via* antisolvent-free and ambient-air processes (45–50% humidity and 25–30 °C). The SnO_2 precursor, Al_2O_3 and $Cu_{\delta}Ni_{1-\delta}O$ NP solutions were spin-coated sequentially on a cleaned FTO substrate at 4000 rpm for 40 s; next, the C–G–$Cu_{\delta}Ni_{1-\delta}O$ composite solution was drop-casted at 6000 rpm on FTO/SnO_2/Al_2O_3/$Cu_{\delta}Ni_{1-\delta}O$ substrates; after that, each step was followed by annealing at 250 °C for 10 min. The pre-heated $MAPbI_{3-x}Cl_x$–$Cu_{\delta}Ni_{1-\delta}O$ mixed solution at 130 °C was then spin-coated on the FTO/SnO_2/Al_2O_3/$Cu_{\delta}Ni_{1-\delta}O$/(C–G–$Cu_{\delta}Ni_{1-\delta}O$ composite) at 1500 rpm for 30 s, followed by annealing at 130 °C for 1.5 h. Finally, Au electrodes were deposited through a shadow mask in a thermal evaporator (QHV-R53) under a high vacuum.

Characterization

The absorption properties and elemental compositions and chemical and electron states of perovskite composites were analyzed with ultraviolet-visible (UV-vis, DektakXT) spectroscopy and X-ray photoelectron spectroscopy (XPS). The perovskite device configuration was examined *via* field emission scanning electron microscopy (FE-SEM, FEI Apreo LoVac). Perovskite composite bonds were analyzed *via* Fourier transform infrared (IR) transmittance measurements. The performance parameters of PSCs were measured with a solar simulator with a source meter (Keithley series 2400) at 100 mW cm^{-2} under AM 1.5 illumination, which was calibrated by a silicon reference cell. The dimension of the tested solar cells was 3 cm × 3 cm. The device performances were examined with a 0.16 cm^2 mask/aperture. To understand the electrical characteristics of the devices, electronic impedance spectroscopy (EIS) was performed at 250 mV applied-bias under one sunlight intensity in the range from 1 Hz to 300 kHz.

Conflicts of interest

There are no conflicts to declare.

Acknowledgements

This work was supported by the Fundamental Research Funds for the Central Universities (No. 21620347) and startup fund for young talented person program (No. 88016105) from Jinan University.

References

1 NREL, https://www.nrel.gov/pv/assets/pdfs/best-research-cell-efficiencies.20200925.pdf, accessed on September 25, 2020.

2 B. Cai, Y. Xing, Z. Yang, W.-H. Zhang and J. Qiu, *Energy Environ. Sci.*, 2013, **6**, 1480–1485.

3 E. H. Jung, N. J. Jeon, E. Y. Park, C. S. Moon, T. J. Shin, T.-Y. Yang, J. H. Noh and J. Seo, *Nature*, 2019, **567**, 511–515.

4 X. Meng, Z. Cai, Y. Zhang, X. Hu, Z. Xing, Z. Huang, Z. Huang, Y. Cui, T. Hu, M. Su, X. Liao, L. Zhang, F. Wang, Y. Song and Y. Chen, *Nat. Commun.*, 2020, **11**, 3016.

5 S. S. Mai, H. Kim, S. E. Shim and C. K. Hong, *Nanoscale*, 2016, **8**, 19189–19194.

6 P. Wang, Y. Wu, B. Cai, Q. Ma, X. Zheng and W.-H. Zhang, *Adv. Funct. Mater.*, 2019, **29**, 1807661.

7 J. Hu, C. Wang, S. Qiu, Y. Zhao, E. Gu, L. Zeng, Y. Yang, C. Li, X. Liu, K. Forberich, C. J. Brabec, M. K. Nazeeruddin, Y. Mai and F. Guo, *Adv. Energy Mater.*, 2020, **10**, 2000173.

8 M. He, B. Li, X. Cui, B. Jiang, Y. He, Y. Chen, D. O'Neil, P. Szymanski, M. A. EI-Sayed, J. Huang and Z. Lin, *Nat. Commun.*, 2017, **8**, 16045.

9 H. Chen and S. Yang, *Adv. Mater.*, 2017, **29**, 1603994.

10 K. Lee, J. Kim, H. Yu, J. W. Lee, C.-M. Yoon, S. K. Kim and J. Jang, *J. Mater. Chem. A*, 2018, **6**, 24560–24568.

11 S. He, L. Qiu, D.-Y. Son, Z. Liu, E. J. Juarez-Perez, L. K. Ono, C. Stecker and Y. Qi, *ACS Energy Lett.*, 2019, **4**, 2032–2039.

12 Y. Sheng, A. Mei, S. Liu, M. Duan, P. Jiang, C. Tian, Y. Xiong, Y. Rong, H. Han and Y. Hu, *J. Mater. Chem. A*, 2018, **6**, 2360–2364.

13 A. Mei, X. Li, L. Liu, Z. Ku, T. Liu, Y. Rong, M. Xu, M. Hu, J. Chen, Y. Yang, M. Grätzel and H. Han, *Science*, 2014, **345**, 295–298.

14 P. Liu, Y. Gong, Y. Xiao, M. Su, S. Kong, F. Qi, H. Zhang, S. Wang, X. Sun, C. Wang and X.-Z. Zhao, *Chem. Commun.*, 2019, **5**, 218–221.

15 G. Grancini, C. Roldàn-Carmona, I. Zimmermann, E. Mosconi, X. Lee, D. Martineau, S. Narbey, F. Oswald, F. De Angelis, M. Gräetzel and M. K. Nazeeruddin, *Nat. Commun.*, 2017, **8**, 15684.

16 Y. Wang, W.-Y. Rho, H.-Y. Yang, T. Mahmoudi, S. Seo, D.-H. Lee and Y.-B. Hahn, *Nano Energy*, 2016, **27**, 535–544.

17 Y. Sheng, Y. Hu, A. Mei, P. Jiang, X. Hou, M. Duan, L. Hong, Y. Guan, Y. Rong, Y. Xiong and H. Han, *J. Mater. Chem. A*, 2016, **4**, 16731–16736.

18 X. Hou, Y. Hu, H. Liu, A. Mei, X. Li, M. Duan, G. Zhang, Y. Rong and H. Han, *J. Mater. Chem. A*, 2017, **5**, 73–78.

19 I. Zimmermann, P. Gratia, D. Martineau, G. Grancini, J.-N. Audinot, T. Wirtz and M. K. Nazeeruddin, *J. Mater. Chem. A*, 2019, **7**, 8073–8077.

20 H. Zhang, H. Wang, S. T. Williams, D. Xiong, W. Zhang, C.-C. Chueh, W. Chen and A. K.-Y. Jen, *Adv. Mater.*, 2017, **29**, 1606608.

21 W.-Q. Wu, Q. Wang, Y. Fang, Y. Shao, S. Tang, Y. Deng, H. Lu, Y. Liu, T. Li, Z. Yang, A. Gruverman and J. Huang, *Nat. Commun.*, 2018, **9**, 1625.

22 Y. Xiong, X. Zhu, A. Mei, F. Qin, S. Liu, S. Zhang, Y. Jiang, Y. Zhou and H. Han, *Sol. RRL*, 2018, **2**, 1800002.

23 J. Liu, Q. Zhou, N. K. K. Thein, L. Tian, D. Jia, E. M. J. Johansson and X. Zhang, *J. Mater. Chem. A*, 2019, **7**, 13777–13786.

24 E. Avigad and L. Etgar, *ACS Energy Lett.*, 2018, **3**, 2240–2245.

25 B. Li, Y. Zhang, L. Zhang and L. Yin, *Adv. Mater.*, 2017, **29**, 1701221.

26 X. Zheng, H. Chen, Q. Li, Y. Yang, Z. Wei, Y. Bai, Y. Qiu, D. Zhou, K. S. Wong and S. Yang, *Nano Lett.*, 2017, **17**, 2496–2505.

27 M. Saliba, T. Matsui, K. Domanski, J.-Y. Seo, A. Ummadisingu, S. M. Zakeeruddin, J.-P. Correa-Baena, W. R. Tress, A. Abate, A. Hagfeldt and M. Grätzel, *Science*, 2016, **354**, 206–209.

28 Q. Tai, P. You, H. Sang, Z. Liu, C. Hu, H. L. W. Chan and F. Yan, *Nat. Commun.*, 2016, **7**, 11105.

29 A. D. Jodlowski, C. Roldan-Carmona, G. Grancini, M. Salado, M. Ralaiarisoa, S. Ahmad, N. Koch, L. Camacho, G. de Miguel and M. K. Nazeeruddin, *Nat. Energy*, 2017, **2**, 972–979.

30 Y. Wang, T. Mahmoudi, W.-Y. Rho, H.-Y. Yang, S. Seo, K. S. Bhat, R. Ahmad and Y.-B. Hahn, *Nano Energy*, 2017, **40**, 408–417.

31 Y. Wang, T. Mahmoudi, H.-Y. Yang, K. S. Bhat, J.-Y. Yoo and Y.-B. Hahn, *Nano Energy*, 2018, **49**, 59–66.

32 Y. Wang, T. Mahmoudi, W.-Y. Rho and Y.-B. Hahn, *Nano Energy*, 2019, **64**, 103964.

33 Y. Wang, T. Mahmoudi and Y.-B. Hahn, *Adv. Energy Mater.*, 2020, **10**, 2000967.

34 S. S. Mali, H. Kim, H. H. Kim, S. E. Shim and C. K. Hong, *Mater. Today*, 2018, **21**, 483–500.

35 H.-L. Hsu, H.-T. Hsiao, T.-Y. Juang, B.-H. Jiang, S.-C. Chen, R.-J. Jeng and C.-P. Chen, *Adv. Energy Mater.*, 2018, **8**, 1802323.

36 T. Mahmoudi, Y. Wang and Y.-B. Hahn, *ACS Energy Lett.*, 2019, **4**, 235–241.

37 T. Mahmoudi, Y. Wang and Y.-B. Hahn, *Nano Energy*, 2018, **47**, 51–65.

38 T. Mahmoudi, S. Seo, H.-Y. Yang, W.-Y. Rho, Y. Wang and Y.-B. Hahn, *Nano Energy*, 2016, **28**, 179–187.

39 Y. Liang, Y. Wang, C. Mu, S. Wang, X. Wang, D. Xu and L. Sun, *Adv. Energy Mater.*, 2018, **8**, 1701159.

40 W. Li, W. Zhang, S. V. Reenen, R. J. Sutton, J. Fan, A. A. Haghighirad, M. B. Johnston, L. Wang and H. J. Snaith, *Energy Environ. Sci.*, 2016, **9**, 490–498.

41 T. Leijtens, G. E. Eperon, S. Pathak, A. Abate, M. M. Lee and H. J. Snaith, *Nat. Commun.*, 2013, **4**, 2885.

42 P. Calado, A. M. Telford, D. Bryant, X. Li, J. Nelson, B. C. O'Regan and P. R. F. Barnes, *Nat. Commun.*, 2016, **7**, 13831.

43 Z. Li, C. Xiao, Y. Yang, S. P. Harvey, D. H. Kim, J. A. Christians, M. Yang, P. Schulz, S. U. Nanayakkara, C.-S. Jiang, J. M. Luther, J. J. Berry, M. C. Beard, M. M. Al-Jassim and K. Zhu, *Energy Environ. Sci.*, 2017, **10**, 1234–1242.

44 S. G. Motti, D. Meggiolaro, A. J. Barker, E. Mosconi, C. A. R. Perini, J. M. Ball, M. Gandini, M. Kim, F. D. Angelis and A. Petrozza, *Nat. Photonics*, 2019, **13**, 532–539.

45 L. Liang, Y. Cai, X. Li, M. K. Nazeeruddin and P. Gao, *Nano Energy*, 2018, **52**, 211–238.

46 H. Back, G. Kim, J. Kim, J. Kong, T. K. Kim, H. Kang, H. Kim, J. Lee, S. Lee and K. Lee, *Energy Environ. Sci.*, 2016, **9**, 1258–1263.

47 M. Duan, C. Tian, Y. Hu, A. Mei, Y. Rong, Y. Xiong, M. Xu, Y. Sheng, P. Jiang, X. Hou, X. Zhu, F. Qin and H. Han, *ACS Appl. Mater. Interfaces*, 2017, **9**, 31721–31727.

48 Z. Wu, Z. Liu, Z. Hu, Z. Hawash, L. Qiu, Y. Jiang, L. K. Ono and Y. Qi, *Adv. Mater.*, 2019, **31**, 1804284.

49 Q.-Q. Chu, Z. Sun, B. Ding, K.-S. Moon, G.-J. Yang and C.-P. Wong, *Nano Energy*, 2020, **77**, 105110.

50 G. D. Tainter, T. Horantner, L. M. Pazos-Outon, R. D. Lamboll, H. Abolins, T. Leijtens, S. Mahesh, R. H. Friend, H. J. Snaith, H. J. Joyce and F. Deschler, *Joule*, 2019, **3**, 1301–1313.

51 P. Jiang, Y. Xiong, M. Xu, A. Mei, Y. Sheng, L. Hong, T. W. Jones, G. J. Wilson, S. Xiong, D. Li, Y. Hu, Y. Rong and H. Han, *J. Phys. Chem. C*, 2018, **122**, 16481–16487.

52 T. Mahmoudi, Y. Wang and Y.-B. Hahn, *Adv. Energy Mater.*, 2020, **10**, 1903369.